J. Fluid Mech. (2023), *vol*. 956, R1, doi:10.1017/jfm.2023.2

On low-frequency unsteadiness in swept shock wave–boundary layer interactions

Alessandro Ceci[1],†, **Andrea Palumbo**[1], **Johan Larsson**[2] **and Sergio Pirozzoli**[1]

[1]Dipartimento di Ingegneria Meccanica ed Aerospaziale, Sapienza University of Rome, Via Eudossiana 18, 00184 Rome, Italy

[2]Department of Mechanical Engineering, University of Maryland, College Park, MD 20742, USA

(Received 29 August 2022; revised 15 November 2022; accepted 27 December 2022)

We derive a scaling law for the characteristic frequencies of wall pressure fluctuations in swept shock wave/turbulent boundary layer interactions in the presence of cylindrical symmetry, based on analysis of a direct numerical simulations database. Direct numerical simulations in large domains show evidence of spanwise rippling of the separation line, with typical wavelength proportional to separation bubble size. Pressure disturbances around the separation line are shown to be convected at a phase speed proportional to the cross-flow velocity. This information is leveraged to derive a simple model for low-frequency unsteadiness, which extends previous two-dimensional models (Piponniau *et al.*, *J. Fluid Mech.*, vol. 629, 2009, pp. 87–108), and which correctly predicts growth of the typical frequency with the sweep angle. Inferences regarding the typical frequencies in more general swept shock wave/turbulent boundary layer interactions are also discussed.

Key words: compressible boundary layers, shock waves, turbulence simulation

1. Introduction

Shock wave/turbulent boundary layer interactions (SBLIs) are a typical hallmark of high-speed aerodynamics. Common examples of SBLIs can be found both in external flows, such as transonic/supersonic airfoils, wing–body junctions and aircraft control surfaces, and in internal flows, such as engine supersonic inlets (Smits & Dussauge 2006). Shock impingement on boundary layers often results in extensive reversed flow, with associated low-frequency unsteady pressure loads mainly localized near the separation line as a result of motion of the reflected shock foot. Low-frequency pressure fluctuations pose

† Email address for correspondence: alessandro.ceci@uniroma1.it

serious concerns to aircraft design, as they are prone to trigger fluid–structure interaction phenomena with potential structural damage. As a result, this phenomenon has been extensively studied, and is reviewed in several reference papers (Dolling 2001; Clemens & Narayanaswamy 2014; Gaitonde & Adler 2023).

Most experimental and numerical studies are generally focused on 'two-dimensional' configurations, in which the shock impingement line is orthogonal to the incoming flow. In this canonical set-up, the general consensus is that two main driving mechanisms are responsible for low-frequency unsteadiness (Clemens & Narayanaswamy 2014). For mildly separated flow, unsteadiness is mainly linked to advection of large-scale structures embedded in the incoming boundary layer ('upstream mechanism'; see e.g. Ganapathisubramani, Clemens & Dolling (2009) and Humble *et al.* (2009)). For strongly separated flows, periodic expansion and contraction resulting in 'breathing' of the separation bubble is believed to play a major role ('downstream mechanism'; see e.g. Piponniau *et al.* (2009) and Touber & Sandham (2009)). In practice, the upstream and the downstream mechanisms coexist, their relative importance depending on the strength of the impinging shock (Souverein *et al.* 2009).

A scaling law for low-frequency pressure oscillations in strong interactions was inferred by Dussauge, Dupont & Debiève (2006) based on analysis of existing SBLI data. Specifically, they showed that the typical frequencies scale with the size of the separation bubble (say, L_{sep}) and with the upstream velocity (u_0), resulting in typical Strouhal numbers $St_L = fL_{sep}/u_0 \approx 0.03$–$0.05$. This scaling was later explained by Piponniau *et al.* (2009) as resulting from breathing motion of the separation bubble and associated shear layer flapping along the bubble upper boundary. A possible physical explanation for breathing motion of the separation bubble has recently been offered by Sasaki *et al.* (2021), who found that the only causal inputs that are highly correlated with shock motions reside around and downstream of the recirculation bubble, and envisaged the occurrence of an acoustic feedback loop mechanism as originally argued by Pirozzoli & Grasso (2006).

In practical applications, the shock impingement line is, however, seldom orthogonal to the incoming boundary layer. Depending on the shock strength and the sweep angle, the interaction is characterized by either parallel or diverging separation/reattachment lines along the spanwise direction, which correspond to cylindrical or conical symmetry conditions, respectively (Settles, Perkins & Bogdonoff 1980). This is the case for flows over swept compression ramps (Settles *et al.* 1980; Erengil & Dolling 1993; Vanstone *et al.* 2017; Adler & Gaitonde 2018, 2020), around sharp fins (Schmisseur & Dolling 1994; Gaitonde *et al.* 1999; Arora, Mears & Alvi 2019) and for swept impinging oblique SBLIs (Doehrmann *et al.* 2018; Padmanabhan *et al.* 2021). All the above studies of swept SBLIs agree about the importance of three-dimensional effects on low-frequency unsteadiness, with consensus on an increase of the typical frequencies with the sweep angle.

However, whereas early experimental studies (Erengil & Dolling 1993) suggested a continuously increasing trend with the sweep angle, recent numerical studies (Adler & Gaitonde 2020) rather seem to indicate suppression of the low-frequency peak in the presence of three-dimensional effects, on account of a topological change of the separation bubble from a closed to an open type. Another important issue in swept interactions is the possible variation of the typical frequencies along the spanwise direction. Whereas Erengil & Dolling (1993) suggested a spanwise decrease of the typical frequencies, more recent studies tend to support invariance (Adler & Gaitonde 2020; Padmanabhan *et al.* 2021).

Given this background and the importance of the subject, we believe that a deeper understanding of the physical mechanisms underlying low-frequency unsteadiness in

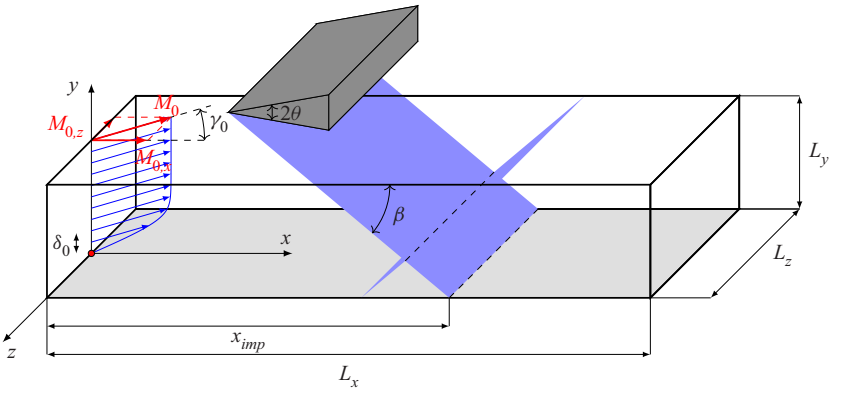

Figure 1. Numerical set-up for swept SBLI analysis. Here δ_0 is the inflow boundary layer thickness, γ_0 is the inflow sweep angle, x_{imp} is the nominal shock impingement position, β is the shock inclination angle and θ is the flow deflection angle.

swept SBLIs is appropriate. For that purpose, we leverage a novel direct numerical simulations (DNS) dataset based on the idealized set-up originally considered by Gross & Fasel (2016) in which both the shock strength and the flow sweep angle are varied. Proper orthogonal decomposition (POD) and frequency–wavenumber spectra of the wall pressure distribution are then used to infer the characteristic length and velocity scales of the problem, based on which a scaling law for the typical frequencies of pressure fluctuations is derived.

2. Computational set-up

The flow set-up replicates that used in previous studies aimed at establishing the effects of cross-flow on SBLIs (Gross & Fasel 2016; Lee & Gross 2021; Di Renzo *et al.* 2022; Larsson *et al.* 2022), as sketched in figure 1. The boundary layer is injected through the inflow plane $x = 0$ with sweep angle γ_0, and an oblique shock wave (β is the shock angle) is introduced by deflecting the flow by an angle θ, which nominally impinges on the boundary layer at $x_{imp} = 64\delta_0$. The x-projected Mach number is kept constant at $M_{0,x} = u_{0,x}/c_0 = 2.28$, where $u_{0,x} = u_0 \cos\gamma_0$ is the x-projected free-stream velocity and c_0 is the free-stream sound speed, resulting in varying free-stream absolute Mach number $M_0 = M_{0,x}/\cos\gamma_0$. Several values of γ_0 and θ have been considered, as listed in table 1. The spanwise size of the computational box (L_z) is varied from $8\delta_0$ (similar to most previous studies, and labelled as NRW) to $96\delta_0$ (much wider than in any previous studies). It turns out that this choice has substantial impact, as discussed next. A mesh with $N_x \times N_y \times N_z = 1920 \times 240 \times 2016$ nodes is used for DNS in large boxes, whereas $N_z = 168$ is used for the NRW cases. The streamwise and wall-normal domain sizes are set to $(L_x \times L_y)/\delta_0 = 96 \times 20$ for all cases.

An in-house solver, available as an open-source code (Bernardini *et al.* 2021), is used for all the DNS. Numerical boundary conditions at the far-field boundaries are managed according to a characteristic relaxation strategy (Pirozzoli & Colonius 2013). The recycling–rescaling procedure is used to generate the target flow at the inflow, as described by Ceci *et al.* (2022). The impinging shock is generated through local enforcement of the Rankine–Hugoniot jump relations at the top boundary, and periodic boundary conditions

Label	M_0	M_{0x}	γ_0 (deg.)	θ (deg.)	Re_{δ_0}	$(L_x \times L_y \times L_z)/\delta_0$	L_{sep}/δ_0	$St_{L,pk}$	$St_{L,min}$
G00_T10_NRW	2.28	2.28	0	10.4	15 800	$96 \times 20 \times 8$	12.11	0.048	0.0069
G30_T10_NRW	2.63	2.28	30	10.4	19 000	$96 \times 20 \times 8$	17.42	0.067	0.0109
G00_T08	2.28	2.28	0	8	15 800	$96 \times 20 \times 96$	4.00	0.041	0.0023
G00_T10	2.28	2.28	0	10.4	15 800	$96 \times 20 \times 96$	12.11	0.041	0.0037
G07_T10	2.30	2.28	7.5	10.4	15 800	$96 \times 20 \times 96$	12.61	0.055	0.0029
G15_T10	2.36	2.28	15	10.4	16 200	$96 \times 20 \times 96$	13.51	0.11	0.0081
G30_T08	2.63	2.28	30	8	19 000	$96 \times 20 \times 96$	5.50	0.18	0.0032
G30_T09	2.63	2.28	30	9.2	19 000	$96 \times 20 \times 96$	10.01	0.22	0.0046
G30_T10	2.63	2.28	30	10.4	19 000	$96 \times 20 \times 96$	17.42	0.22	0.0053
G45_T10	3.22	2.28	45	10.4	27 500	$96 \times 20 \times 96$	47.65	0.38	0.0125

Table 1. Flow parameters for the DNS database: M_0 is the free-stream Mach number, M_{0x} is its x projection, γ_0 is the incoming flow sweep angle, θ is the flow deflection angle, $Re_{\delta_0} = \rho_0 u_0 \delta_0/\mu_0$ is the inflow Reynolds number, L_x, L_y, L_z is the size of the computational box, L_{sep} is the separation bubble extent, and $St_{L,pk}$ and $St_{L,min}$ are the peak and the minimum resolved Strouhal numbers and T is the time window used for the spectral analysis. The suffix NRW refers to DNS carried out in narrow domains ($L_z = 8\delta_0$).

are applied to the spanwise boundaries. The wall is assumed to be isothermal, with temperature set to the nominal adiabatic value.

Averaging is started after statistically steady conditions are established, as estimated by monitoring the time history of the spanwise-averaged separation point. The minimum resolved Strouhal numbers ($St_{min} = L_{sep}/(u_{0,x}T)$, where T is the time window for the statistical analysis) are reported in table 1. The time window may seem marginal for some of the flow cases, especially the G45_T10 case, in which it would correspond to slightly less than three fundamental cycles if the typical Strouhal number was $St \approx 0.03$. However, one of the key results of the present study – see figure 8(a) and related discussion – is that the peak Strouhal number (also reported in table 1) increases significantly with the skew angle, hence the effective number of resolved low-frequency cycles is much higher. The spectra hereafter reported have been obtained by sampling the data at time intervals $\Delta t = 0.27\delta_0/u_{0,x}$, and using the Welch method by splitting the signal into eight segments with 50 % overlap, upon use of Hamming windowing. The same samples are used also for the POD analysis, which we carry out following Sirovich (1987).

3. Analysis

The effect of the spanwise width on some basic flow properties (namely, friction coefficient and wall pressure variance) is addressed in figure 2. As shown in previous studies (Di Renzo *et al.* 2022; Larsson *et al.* 2022), the presence of a non-zero sweep angle yields substantial enlargement of the interaction zone, as compared to the case of two-dimensional, non-swept interactions. However, the effect of the domain width is very limited, in both cases. Maps of the power spectral density (PSD) of wall pressure are shown in figure 3, normalized by the respective variances ($\hat{E}(f)$), in pre-multiplied form. Consistent with the general wisdom, the non-swept case shows the occurrence of low-frequency dynamics at $10^{-2} \lesssim St_L \lesssim 10^{-1}$, in a limited space interval around the mean separation point. No obvious effect of the spanwise domain size is visible in that case, although, of course, the spectra collected in the wider domains are smoother as a

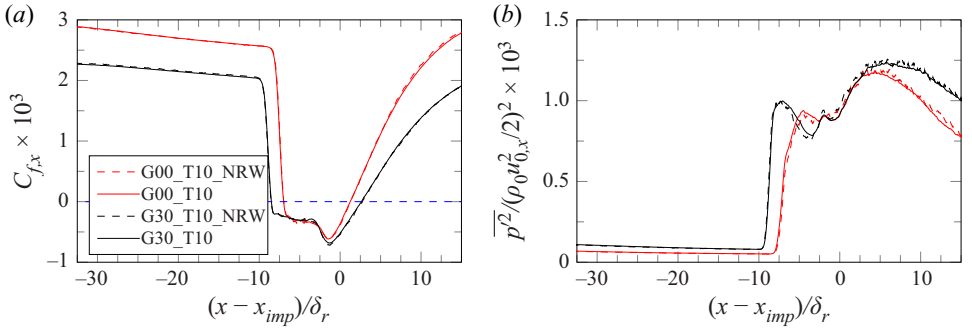

Figure 2. Distributions of x-projected friction coefficient (a) and wall pressure variance (b). Solid lines denote DNS in the widest domain ($L_z = 96\delta_0$), and dashed lines denote DNS in the narrowest domain ($L_z = 8\delta_0$). In both cases the deviation angle is $\theta = 10.4^\circ$. Two-dimensional cases ($\gamma_0 = 0^\circ$) are coloured in red, and swept cases (with $\gamma_0 = 30^\circ$) are coloured in black. The streamwise coordinate is scaled by the boundary layer thickness δ_r upstream of the mean separation line.

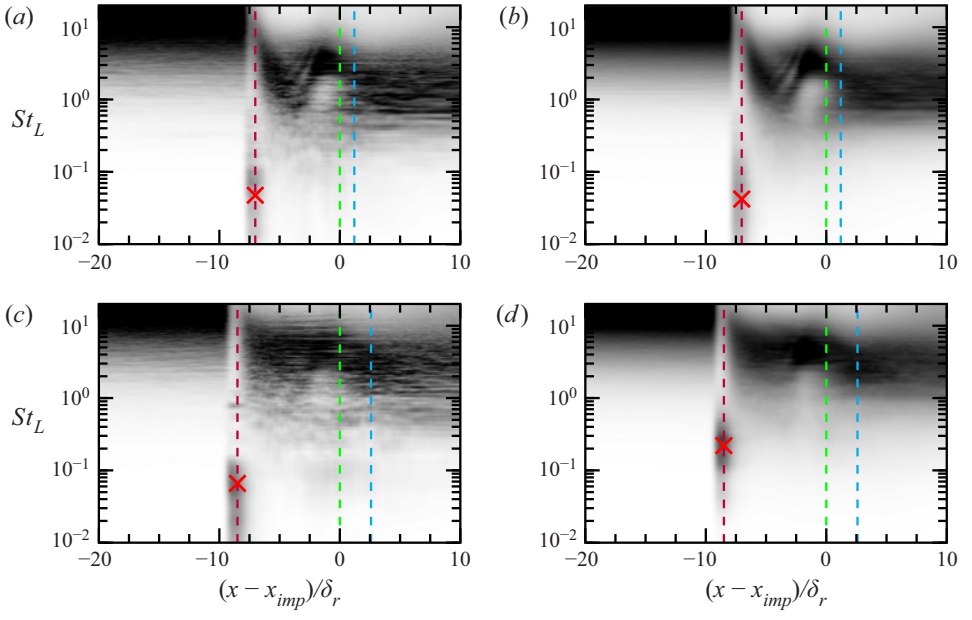

Figure 3. Pre-multiplied normalized PSD of wall pressure for flow cases G00_Lz08 (a), G00_Lz96 (b), G30_Lz08 (c) and G30_Lz96 (d). In all cases $\theta = 10.4^\circ$. The red/purple line denotes the mean separation location, the green line the nominal shock impingement location, and the cyan line the mean reattachment location. Red crosses mark the position of the low-frequency peaks near the separation line. Spectra are also averaged in the spanwise direction.

result of averaging in the spanwise direction. The swept case in small domains (figure 3c) also shows a similar pattern, on account of previously noted differences in the size of the interaction zone. Quite surprisingly, DNS of the swept case in a large domain (figure 3d) shows substantial increase of the peak frequency, which was the original motivation for further analysis.

After discarding possible effects related to spurious flow periodicity along the spanwise direction, which are discussed in Larsson *et al.* (2022), we turned to analyse the spatial

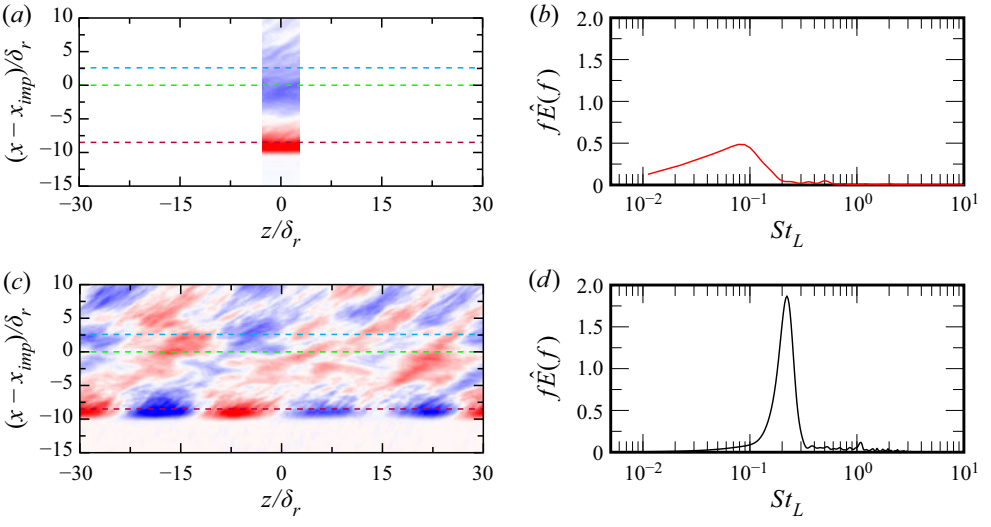

Figure 4. Shape of leading POD mode of wall pressure (*a*,*c*) and pre-multiplied normalized PSD of the corresponding temporal coefficient (*b*,*d*): (*a*,*b*) G30_T10_NRW ($\gamma_0 = 30^\circ$, $L_z = 8\delta_0$); and (*c*,*d*) G30_T10 ($\gamma_0 = 30^\circ$, $L_z = 96\delta_0$). The dashed lines are as in figure 3. In all cases, $\theta = 10.4^\circ$.

pattern of the wall pressure through POD. Figure 4 depicts the shape of the most energetic POD modes for $\gamma_0 = 30^\circ$, in small and large domains, along with their associated PSD. The leading POD mode in the small domain features a spanwise-invariant distribution, with a sharp peak at the mean separation line, and a flatter distribution with opposite sign at reattachment, hence overall reminiscent of bubble breathing. The PSD of the associated temporal coefficient in fact has a peak at $St_L \approx 0.07$–0.08, which is very close to the peak value of the pressure PSD in figure 3(*c*). The leading POD mode in the $L_z = 96\delta_0$ box is instead characterized by apparent spanwise corrugation around the mean separation line, and by oblique structures stretching up to the reattachment line. The PSD of the associated temporal coefficient peaks at $St_L \approx 0.21$–0.22, which is very close to the peak frequency of the temporal PSD at the separation line in figure 3(*d*). Similar conclusions apply to all cases under scrutiny, including non-swept ones. We find that rippling of the separation line is visible only if sufficiently wide boxes are used, as we have checked with DNS in domains with intermediate size $L_z = \{24, 32, 64\}\delta_0$, not shown here.

In order to quantitatively characterize the observed rippling of the separation line, in figure 5 we show the PSD of the wall pressure as a function of the spanwise wavelength, scaled either by the incoming boundary layer thickness or by the length of the separation bubble. We argue that marginally better collapse of the PSD across the γ_0 range is achieved in the latter case, especially for the extreme $\gamma_0 = 45^\circ$ case, which exhibits massive flow separation, and for which even the largest box used here may be barely sufficient. Two spectral peaks are observed, one at small wavelength ($\lambda_z \approx 0.1L_{sep}$), which would probably correspond to the small-scale rippling noticed in previous numerical simulations of non-swept SBLIs (Pasquariello, Hickel & Adams 2017). However, the most prominent peak is found to reside at much longer wavelengths ($\lambda_z \approx 2L_{sep}$), which cannot be resolved in numerical simulations in small boxes.

Wavenumber–frequency spectra at the mean separation line are further considered in figure 6 to characterize the advection velocity of pressure disturbances. Whereas no clear organization is observed in non-swept SBLIs (figure 6*a*), distinct clustering of

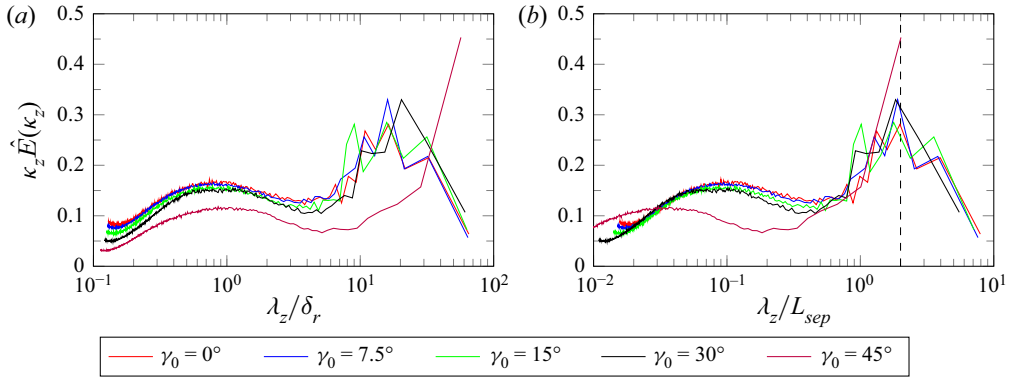

Figure 5. Spanwise pre-multiplied normalized PSD of wall pressure at the mean separation line for various sweep angles γ_0 at fixed shock strength ($\theta = 10.4°$). The spanwise wavelength λ_z is scaled with either (*a*) the reference boundary layer thickness δ_r or (*b*) the separation length. Here $\kappa_z = 2\pi/\lambda_z$ is the spanwise wavenumber. The dashed line in panel (*b*) marks $\lambda_z = 2L_{sep}$.

the PSD around a linear distribution is found in swept interactions, which becomes more evident at high sweep angles, and which is a clear indication of the presence of convecting disturbances. In particular, data fitting yields $\omega = w_c\kappa_z$, with convection velocity proportional to the cross-flow free-stream velocity, namely $w_c \approx 0.7u_{0,z} = 0.7u_{0,x}\tan\gamma_0$.

4. Model synthesis

Based on the above evidence, we are led to formulate a tentative model for the behaviour of pressure fluctuations near the separation line in swept SBLIs, as sketched in figure 7. Specifically, we assume that the separation line oscillates sinusoidally in space with wavelength $\lambda_z = \alpha L_{sep}$ and in time with frequency f_0, such that $St_{L,0} = f_0 L_{sep}/u_{0,x}$ is the typical Strouhal number for two-dimensional breathing. Further assuming that pressure disturbances are convected along the z direction at speed $w_c = \eta u_{0,x}\tan\gamma_0$, the behaviour of pressure fluctuations along the shock foot can be described as

$$\begin{aligned} p'(z,t) &\sim \exp(\pm \mathrm{i}2\pi f_0 t)\exp(\pm \mathrm{i}2\pi(z - w_c t)/\lambda_z) \\ &= \exp(\pm \mathrm{i}2\pi z/\lambda_z)\exp(\mathrm{i}2\pi t(\pm f_0 \mp w_c/\lambda_z)), \end{aligned} \tag{4.1}$$

which implies that the typical non-dimensional frequency of oscillation in swept SBLIs is

$$St_L = \left| St_{L,0} \pm \frac{\eta\tan\gamma_0}{\alpha} \right|, \tag{4.2}$$

with $\alpha \approx 2$ and $\eta \approx 0.7$, as obtained from the previous analysis, and $St_{L,0} \approx 0.04$.

Figure 8(*a*) shows the pre-multiplied pressure PSD at the separation line for fixed shock strength and increasing sweep angle. The figure also shows the frequency spectra using a 50 % shorter time window for the cases G00_T10, G30_T10 and G45_T10. All distributions exhibit a bump at the high-frequency end, which is associated with the boundary layer turbulence dynamics. In addition, they show prominent peaks at much lower frequency, which, however, are shifted to the right and increase in magnitude as the sweep angle grows. Although some difference may be spotted (especially for the G45_T10 flow case), we can confidently state that the limited duration of the time window

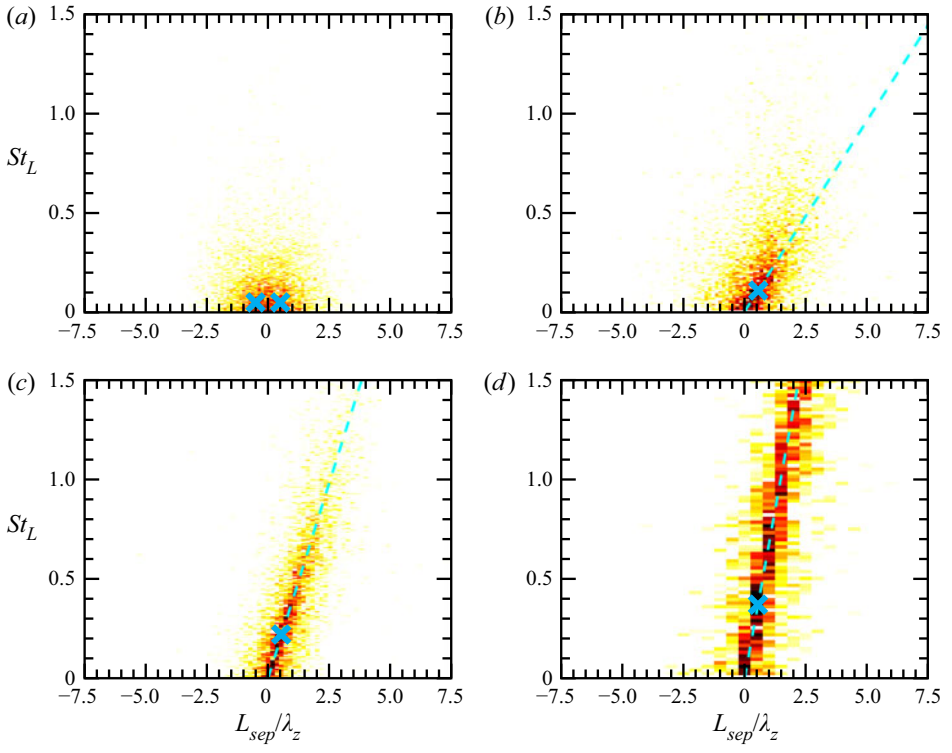

Figure 6. Contour plots of spanwise wavenumber–frequency spectra of wall pressure at the mean separation location. Dashed lines denote the linear relationship $\omega = \kappa_z w_c$, with convection velocity $w_c = 0.7u_{0,x} \tan\gamma_0$: (*a*) $\gamma_0 = 0°$; (*b*) $\gamma_0 = 15°$; (*c*) $\gamma_0 = 30°$; and (*d*) $\gamma_0 = 45°$. In all cases $\theta = 10.4°$. The blue crosses mark the position of the low-frequency peaks.

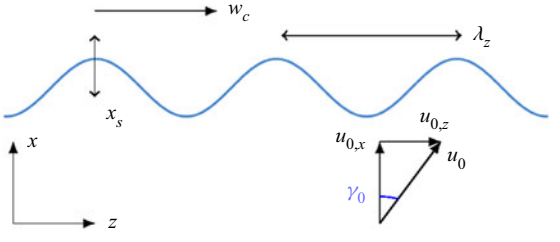

Figure 7. Sketch of envisaged oscillation of the separation line. Here x_s is the x coordinate of the separation line, w_c is the spanwise convection velocity, and λ_z is the wavelength of the spanwise corrugations.

does not affect the typical frequencies, and energy at the expected 'two-dimensional' characteristic frequency ($St_L = 0.03$–0.04) is negligible in cases with significant skewing of the flow. The model in (4.2) predicts two distinct frequencies, but one should regard those as broadband peaks that could well merge into one if sufficiently wide. Quantitative comparison of the numerically computed peak frequencies with the prediction of (4.2) is presented in figure 8(*b*), in which we also include results of DNS with different shock strength. The prediction is clearly quite good, perhaps with exception of the single data point corresponding to $\gamma_0 = 30°$, $\theta = 8°$, which features a relatively small separation bubble. Overall, we find that the agreement becomes more satisfactory as the sweep angle

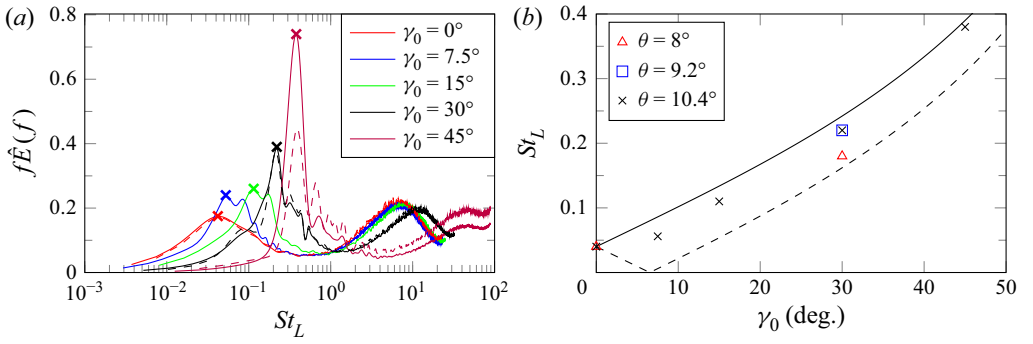

Figure 8. (*a*) Pre-multiplied normalized frequency spectra of wall pressure at the mean separation line for various sweep angles and for fixed shock strength ($\theta = 10.4°$). Peaks are marked with crosses. Solid lines denote PSD obtained with the full time window, whereas dashed lines denote PSD obtained with 50 % shorter time windows. (*b*) Peak frequency as a function of sweep angle: the solid and dashed lines denote the prediction of (4.2).

increases, which is consistent with stronger coherence of convecting pressure disturbances noticed when discussing figure 6.

5. Discussion

We have developed a simple model to characterize low-frequency unsteadiness in swept SBLIs, which is robustly supported from analysis of DNS data. Although at the present stage we cannot offer a complete mechanistic justification for our observations, we provide a scaling law for the spanwise undulation of the separation line and for the convection velocity of pressure disturbances, which concur to predict growth of the typical pressure oscillation frequency with the skew angle, consistent with trends observed in DNS. One should, of course, bear in mind that the present database refers to the idealized case of a statistically two-dimensional flow with addition of cross-flow, which is representative of SBLIs with cylindrical symmetry (Gross & Fasel 2016).

However, SBLIs in practical occurrences almost invariably feature conical symmetry. Hence, a crucial question is whether and to what extent our findings and predictions actually apply to realistic occurrences of swept SBLIs. In this respect we note that the two key elements which we have identified as being responsible for the observed low-frequency unsteadiness, namely spanwise undulation of the separation line and convection of pressure disturbances, have been observed previously in several studies of swept SBLIs. In fact, the presence of ripples in the instantaneous separation line was first pinpointed in the studies of Vanstone *et al.* (2017) and Vanstone & Clemens (2019). They found that these structures move at approximately 70–80 % of the cross-stream velocity, hence well in line with the present study. However, they reported the typical width of the ripples to be approximately half the incoming boundary layer thickness, hence much less than we find here, and to contribute to a relatively high-frequency range of pressure fluctuations.

Rippling of the separation line was also noticed by Doehrmann *et al.* (2018), Adler & Gaitonde (2020) and Padmanabhan *et al.* (2021). The latter study reports that the rippling motion is associated with low-frequency dynamics at spanwise-constant characteristic frequency, and that it corresponds to disturbances being advected at speed increasing with the spanwise distance, hence with increasing wavelength. A rather unconsolidated scenario emerges, which can be partially explained with effects of incomplete similarity in SBLIs with conical symmetry, and/or with differences from one SBLI case to another.

If the results of the present study are extended directly to swept interactions with conical symmetry on a station-by-station basis, one would infer that undulations of the separation line should have a wavelength proportional to the distance from the virtual origin, and be convected at constant speed. The resulting low-frequency peak would then scale with the local separation bubble size, and the peak frequency should decrease with the spanwise distance. Whereas this scenario is fully consistent with the findings of Erengil & Dolling (1993), it is a bit hard to reconcile it with more recent experiments (Padmanabhan *et al.* 2021).

It should finally be mentioned that only few experimental and numerical studies of swept SBLIs cover a wide range of sweep angles, including small ones. In fact, Erengil & Dolling (1993) noted that '... increase in dominant frequencies is initially small as the interaction is swept from 0 to 20° but becomes more rapid with increasing sweep (25°)'. Hence, additional studies in the range of small sweep angles would be desirable to establish whether the change from two- to three-dimensional dynamics is continuous, or characterized by a sharp transition.

Acknowledgements. We acknowledge that the results reported in this paper have been achieved with computational resources from PRACE Research Infrastructure resource MARCONI100 based at CINECA, Casalecchio di Reno, Italy. A.C. wishes to acknowledge Lionel Larchevêque for support and useful discussions during a secondment at the University of Aix-Marseille.

Funding. This work was supported by TEAMAero Horizon 2020 research and innovation programme under grant agreement 860909 and by the Air Force Office of Scientific Research under grants FA9550-19-1-0210 and FA9550-19-1-7029.

Declaration of interests. The authors report no conflict of interest.

Data availability statement. The datasets generated during and/or analysed during the current study are available from the corresponding author on reasonable request.

Author ORCIDs.
Alessandro Ceci https://orcid.org/0000-0001-6664-1677;
Andrea Palumbo https://orcid.org/0000-0003-1042-3931;
Johan Larsson https://orcid.org/0000-0001-8387-1933;
Sergio Pirozzoli https://orcid.org/0000-0002-7160-3023.

References

Adler, M.C. & Gaitonde, D.V. 2018 Unsteadiness in shock/turbulent-boundary-layer interactions with open flow separation. In *2018 AIAA Aerospace Sciences Meeting*. *AIAA Paper* 2018-2075.

Adler, M.C. & Gaitonde, D.V. 2020 Dynamics of strong swept-shock/turbulent-boundary-layer interactions. *J. Fluid Mech.* **896**, A29.

Arora, N., Mears, L. & Alvi, F.S. 2019 Unsteady characteristics of a swept-shock/boundary-layer interaction at Mach 2. *AIAA J.* **57**, 4548–4559.

Bernardini, M., Modesti, D., Salvadore, F. & Pirozzoli, S. 2021 STREAmS: a high-fidelity accelerated solver for direct numerical simulation of compressible turbulent flows. *Comput. Phys. Commun.* **263**, 107906.

Ceci, A., Palumbo, A., Larsson, J. & Pirozzoli, S. 2022 Numerical tripping of high-speed turbulent boundary layers. *Theor. Comput. Fluid Dyn.* **36**, 865–886.

Clemens, N.T. & Narayanaswamy, V. 2014 Low-frequency unsteadiness of shock wave/turbulent boundary layer interactions. *Annu. Rev. Fluid Mech.* **46**, 469–492.

Di Renzo, M., Oberoi, N., Larsson, J. & Pirozzoli, S. 2022 Crossflow effects on shock wave/turbulent boundary layer interactions. *Theor. Comput. Fluid Dyn.* **36**, 327–344.

Doehrmann, A.C., Padmanabhan, S., Threadgill, J.A. & Little, J.C. 2018 Effect of sweep on the mean and unsteady structures of impinging shock/boundary layer interactions. In *2018 AIAA Aerospace Sciences Meeting*. *AIAA Paper* 2018-2074.

DOLLING, D.S. 2001 Fifty years of shock-wave/boundary-layer interaction research: what next? *AIAA J.* **39**, 1517–1531.

DUSSAUGE, J.-P., DUPONT, P. & DEBIÈVE, J.-F. 2006 Unsteadiness in shock wave boundary layer interactions with separation. *Aerosp. Sci. Technol.* **10**, 85–91.

ERENGIL, M.E. & DOLLING, D.S. 1993 Effects of sweepback on unsteady separation in Mach 5 compression ramp interactions. *AIAA J.* **31**, 302–311.

GAITONDE, D.V. & ADLER, M.C. 2023 Dynamics of three-dimensional shock-wave/boundary-layer interactions. *Annu. Rev. Fluid Mech.* **55**, 291–321.

GAITONDE, D.V., SHANG, J.S., GARRISON, T.J., ZHELTOVODOV, A.A. & MAKSIMOV, A.I. 1999 Three-dimensional turbulent interactions caused by asymmetric crossing-shock configurations. *AIAA J.* **37**, 1602–1608.

GANAPATHISUBRAMANI, B., CLEMENS, N.T. & DOLLING, D.S. 2009 Low-frequency dynamics of shock-induced separation in a compression ramp interaction. *J. Fluid Mech.* **636**, 397–425.

GROSS, A. & FASEL, H.F. 2016 Numerical investigation of shock boundary-layer interactions. In *54th AIAA Aerospace Sciences Meeting*. *AIAA Paper* 2016-0347.

HUMBLE, R.A., ELSINGA, G.E., SCARANO, F. & VAN OUDHEUSDEN, B.W. 2009 Three-dimensional instantaneous structure of a shock wave/turbulent boundary layer interaction. *J. Fluid Mech.* **622**, 33–62.

LARSSON, J., KUMAR, V., OBEROI, N., DI RENZO, M. & PIROZZOLI, S. 2022 Large eddy simulations of idealized shock/boundary-layer interactions with crossflow. *AIAA J.* **60**, 2767–2779.

LEE, S. & GROSS, A. 2021 Numerical investigation of sweep effect on turbulent shock-wave boundary-layer interaction. *AIAA J.* **60**, 1–19.

PADMANABHAN, S., MALDONADO, J.C., THREADGILL, J.A.S. & LITTLE, J.C. 2021 Experimental study of swept impinging oblique shock/boundary-layer interactions. *AIAA J.* **59**, 140–149.

PASQUARIELLO, V., HICKEL, S. & ADAMS, N.A. 2017 Unsteady effects of strong shock-wave/boundary-layer interaction at high Reynolds number. *J. Fluid Mech.* **823**, 617–657.

PIPONNIAU, S., DUSSAUGE, J.P., DEBIÈVE, J.F. & DUPONT, P. 2009 A simple model for low-frequency unsteadiness in shock-induced separation. *J. Fluid Mech.* **629**, 87–108.

PIROZZOLI, S. & COLONIUS, T. 2013 Generalized characteristic relaxation boundary conditions for unsteady compressible flow simulations. *J. Comput. Phys.* **248**, 109–126.

PIROZZOLI, S. & GRASSO, F. 2006 Direct numerical simulation of impinging shock wave turbulent boundary layer interaction at $M = 2.25$. *Phys. Fluids* **18**, 065113.

SASAKI, K., BARROS, D.C., CAVALIERI, A.V.G. & LARCHEVÊQUE, L. 2021 Causality in the shock wave/turbulent boundary layer interaction. *Phys. Rev. Fluids* **6**, 064609.

SCHMISSEUR, J.D. & DOLLING, D.S. 1994 Fluctuating wall pressures near separation in highly swept turbulent interactions. *AIAA J.* **32**, 1151–1157.

SETTLES, G.S., PERKINS, J.J. & BOGDONOFF, S.M. 1980 Investigation of three-dimensional shock/boundary-layer interactions at swept compression corners. *AIAA J.* **18**, 779–785.

SIROVICH, L. 1987 Turbulence and the dynamics of coherent structures. I. Coherent structures. *Q. Appl. Maths* **45**, 561–571.

SMITS, A.J. & DUSSAUGE, J.-P. 2006 *Turbulent Shear Layers in Supersonic Flow*. Springer Science & Business Media.

SOUVEREIN, L., DUPONT, P., DEBIÈVE, J.-F., DUSSAUGE, J.-P., VAN OUDHEUSDEN, B. & SCARANO, F. 2009 Effect of interaction strength on the unsteady behavior of shock wave boundary layer interactions. In *39th AIAA Fluid Dynamics Conference. AIAA Paper* 2009-3715.

TOUBER, E. & SANDHAM, N.D. 2009 Large-eddy simulation of low-frequency unsteadiness in a turbulent shock-induced separation bubble. *Theor. Comput. Fluid Dyn.* **23**, 79–107.

VANSTONE, L. & CLEMENS, N.T. 2019 Proper orthogonal decomposition analysis of swept-ramp shock-wave/boundary-layer unsteadiness at Mach 2. *AIAA J.* **57**, 3395–3409.

VANSTONE, L., SALEEM, M., SECKIN, S. & CLEMENS, N.T. 2017 Role of boundary-layer on unsteadiness on a Mach 2 swept-ramp shock/boundary-layer interaction using 50 kHz PIV. In *55th AIAA Aerospace Sciences Meeting*. *AIAA Paper* 2017-0757.